The Influence of In Situ Anatase Particle Addition on the Formation and Properties of Multifunctional Plasma Electrolytic Oxidation Coatings on AA2024 Aluminum Alloy

Stefan Ignjatović, Carsten Blawert, Maria Serdechnova,* Sergey Karpushenkov, Milan Damjanović, Polina Karlova, Gleb Dovzhenko, D. C. Florian Wieland, Berit Zeller-Plumhoff, Maksim Starykevich, Srna Stojanović, Ljiljana Damjanović-Vasilić, and Mikhail L. Zheludkevich

Plasma electrolytic oxidation (PEO) with in situ anatase particle addition is applied to functionalize the surface of AA2024 alloy. A base potassium titanium oxide oxalate dihydrate aqueous electrolyte is used with up to 30 g L^{-1} anatase particle addition. The coatings' morphology and phase composition as a function of the anatase concentration in the electrolyte are characterized by scanning electron microscopy (SEM), X-ray diffraction (XRD), and glow discharge optical emission spectroscopy (GDOES). Photocatalytic activity, stability in chloride solution, and tribological properties are also determined. The main coating forming phases are anatase and rutile on top of a mixed interface region consisting of TiAl$_2$O$_5$ as reaction product between the TiO$_2$ and an Al$_2$O$_3$ barrier layer on top of the Al substrate. The mixed layer is extending with increasing amount of particles added, due to intensified discharges. In addition, anatase-to-rutile phase ratio increases due to the additional anatase particles in the electrolyte. Thus, the photocatalytic activity is improving with the particle addition. The coatings' mechanical resistance is dropping first before increasing again with more particles added. Chemical and restored mechanical stability seems to be related to the extended mixed interface formation, which strengthens the bond to the substrate when more particles are added.

1. Introduction

Plasma electrolytic oxidation (PEO), also known as microarc oxidation or anodic spark deposition, is an environmentally friendly surface engineering technology, used to produce oxide coatings on the surface of lightweight metals (aluminum, magnesium, titanium, etc.) and their alloys. Apart from being an environmentally friendly technology, PEO offers the possibility to avoid expensive equipment required for competing vacuum-based plasma technologies,[1] so the coating growth mechanisms in the PEO process, as well as the coating's microstructure and properties, are gaining more attention.[2–4] PEO coatings improve the electrical insulation properties, wear, and corrosion resistance of metal and alloy surfaces and can be used to create multifunctional coatings.[5–18]

Titania (TiO$_2$) coatings are such multifunctional layers, which combine good chemical stability, photocatalytic activity as well as good tribological and corrosion protection.[19–23] Considering PEO treatments, the formation of TiO$_2$ has been mainly reported for Ti–6Al–4V, for biomedical applications in prosthetic implants,[24–26] but there are only few studies about the formation of TiO$_2$ layers on an aluminum surface by PEO.[27,28] Many articles describe the structure of the PEO coatings on light metal alloys as a multiple layer system—typically a triple layer consisting of a very thin, but dense barrier layer, a moderately porous intermediate layer, and a very porous outer layer.[6] The pores of the outer layer

S. Ignjatović, M. Damjanović
Laboratory for Agrochemicals
Chemical Agrosava
Krnješevačka bb, Šimanovci 22310, Serbia

The ORCID identification number(s) for the author(s) of this article can be found under https://doi.org/10.1002/adem.202001527.

Dr. C. Blawert, Dr. M. Serdechnova, P. Karlova, Prof. M. L. Zheludkevich
Institute of Surface Science
Helmholtz-Zentrum Geesthacht
Max-Planck-Straβe 1, Geesthacht 21502, Germany
E-mail: maria.serdechnova@hzg.de

Dr. S. Karpushenkov
Faculty of Chemistry
Belarusian State University
Nezavisimosti Avenue 4, Minsk 220030, Belarus

Dr. G. Dovzhenko
Institute of Materials Physics
Helmholtz-Zentrum Geesthacht
Max-Planck Straße. 1, Geesthacht 21502, Germany

can be impregnated with catalytic particles, such as TiO_2 (in the form of anatase polymorph) which is one of the most widely used photocatalyst, as it causes the degradation of various organic pollutants under UV light irradiation.[19,20] UV light is required due to its relatively wide bandgap (≈ 3.2 eV for anatase). Furthermore, addition of micro/nanosized particles to the electrolyte in the PEO process can significantly influence the properties of the coating layers, as sealing of the coating defects and reduction of porosity is quite often observed, which positively affects corrosion resistance, thermomechanical, magnetic, catalytic, and bioactive properties of the coatings.[13,29] The effects of different types of additives on morphology, phase composition, structure, thickness, hardness, and other properties have been investigated.[16,30–32] Depending on the nature of the particles, they can undergo various kinds of transformations inside the coating during the plasma microdischarges, such as melting, phase transformation, or reactive formation of new compounds with other parts of the coating while they are more or less uniformly distributed across the coating. A uniform dispersion of the particles in the electrolyte by agitation of the electrolyte either mechanically, ultrasonically, or blowing compressed air[33] is required to reach this uniform distribution. In a previous study, it was demonstrated that TiO_2 coatings can be produced directly on an Al substrate in a PEO process and that anatase particle addition (5 g L^{-1}) can influence the anatase to rutile ratio of the coatings positively.[34] However, the amount of anatase in the coating was still too low to generate sufficient photocatalytic activity. Thus, in the current study the aim was to understand how much anatase particles can be added to the electrolyte before PEO processing becomes unstable and how the increasing amount of particles influences the coating formation and the properties of the coatings. Furthermore, a possible application as photoactive surfaces for waste water cleaning should be verified.

2. Results

2.1. PEO Processing (Voltage–Time Response)

In the standard electrolyte, the size and color of microdischarges are changing throughout the PEO process in the same way as already described in previous study.[34] They appear ≈ 20–30 s after the beginning of the PEO process at a breakdown voltage of around 290 ± 10 V at the end of stage 1 (**Figure 1**). Throughout stage 2, their color turns from white to yellow/orange with increasing discharge energy (voltage). In the final stage 3, the voltage increase is slow and the size of microdischarges becomes larger with increasing time of PEO, while their population
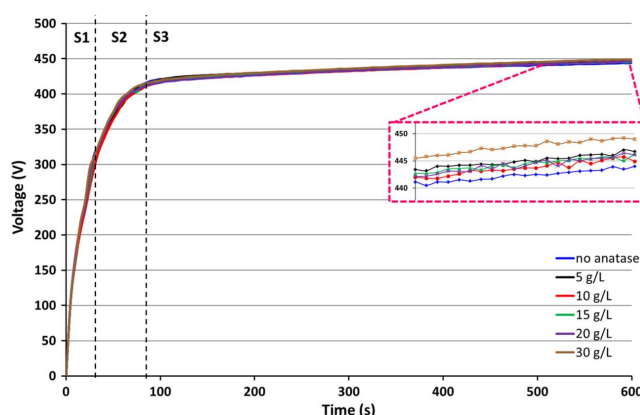
Figure 1. Voltage–time response for PEO processes with 0, 5, 10, 15, 20, and 30 g anatase particles addition.

Table 1. Final voltages after 10 min of PEO treatments.

Electrolyte	Final voltage [V]
No anatase	444.4 ± 2.6
5 g L^{-1} anatase	446.7 ± 2.7
10 g L^{-1} anatase	444.9 ± 1.8
15 g L^{-1} anatase	446.3 ± 3.1
20 g L^{-1} anatase	446.1 ± 2.4
30 g L^{-1} anatase	449.0 ± 2.8

decreases. However, with the addition of particles and their increasing concentrations, it becomes impossible to observe the discharges because of the electrolyte turbidity. However, as the voltage–time response is not changing remarkably, it can be assumed that the discharges are most likely not affected much. Overall, the nanoparticle addition had a relatively minor influence on the voltage–time response, as well as on the final voltages at the end of the processes (**Table 1**). The voltage increased rapidly at the beginning of the oxidation process, reaching 400 V after about 65–70 s, 420 V after 100 s, and followed by a slow increase to the final voltage at 600 s, as shown in Figure 1.

2.2. Surface Morphology, Roughness, and Composition

PEO coatings are characterized by a rough porous surface morphology. This is a consequence of plasma microdischarges causing repetitive melting and solidification of the outer layer, but also of gas bubbles entrapped in the coating. **Figure 2** shows

Dr. D. C. F. Wieland, Dr. B. Zeller-Plumhoff
Institute of Metallic Biomaterials
Helmholtz-Zentrum Geesthacht
Max-Planck Straße. 1, Geesthacht 21502, Germany

Dr. M. Starykevich
Department of Materials and Ceramic Engineering
CICECO – Aveiro Institute of Materials
University of Aveiro
Aveiro 3810-193, Portugal

S. Stojanović, Prof. L. Damjanović-Vasilić
Faculty of Physical Chemistry

University of Belgrade
Studentski trg 12-16, Belgrade 11000, Serbia

Prof. M. L. Zheludkevich
Institute for Materials Science
Faculty of Engineering
University of Kiel
Kaiserstraße 2, Kiel 24143, Germany

2001527 (2 of 17)
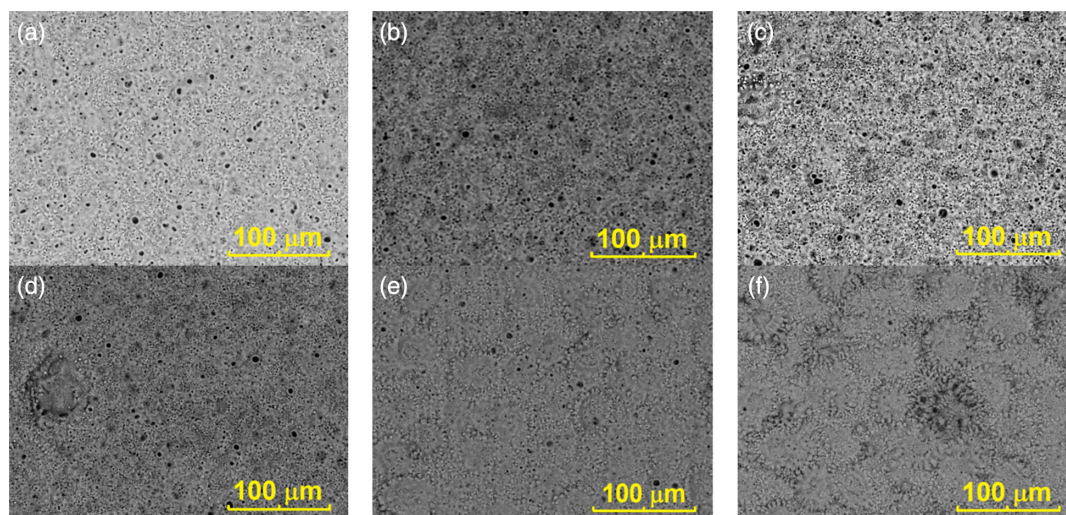
Figure 2. Surface morphology pictures of PEO coatings formed with different amounts of anatase particles addition, taken by SEM—a) $0\,g\,L^{-1}$; b) $5\,g\,L^{-1}$; c) $10\,g\,L^{-1}$; d) $15\,g\,L^{-1}$; e) $20\,g\,L^{-1}$; and f) $30\,g\,L^{-1}$.

the surface morphologies of the coatings prepared without and with anatase particle addition. It is obvious that the coatings had quite different surface morphologies with different amounts of anatase particles added to the electrolyte.

Pores of different sizes and shapes were observed on all coated samples. Especially the open pores are the remains of "solidified" discharge channels. Addition of higher amounts of anatase particles results in fewer pores, as anatase particles can partly seal the pores under certain discharge conditions and particle concentrations, as shown in Figure 2. With increasing amount of particles, the surface morphology is changing (Figure 2). At lower concentrations, the more classical PEO morphology is dominating with its crater-like discharge channels and entrapped gas bubbles, which are produced during the process (**Figure 3**b). With higher concentrations ($>10\,g\,L^{-1}$) more and more flower-like nodular structures are visible (Figure 3c). Those structures are most likely a product of anatase particles being melted and sintered together, covering larger areas and

acting as pore/crater plugs. More of these circular structures appear when higher amounts of anatase particles are introduced to the electrolyte. In previous study, those circular structures were related to surface discharges stimulated by gas bubbles sticking for longer periods at the same position on the surface.[34]
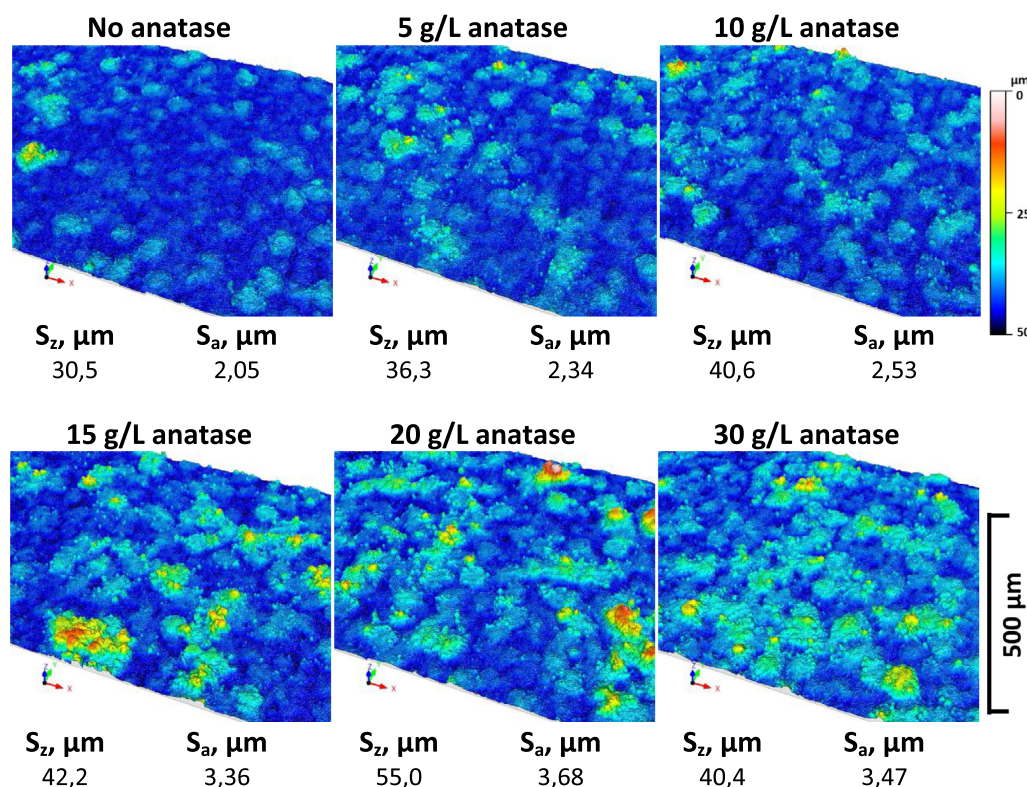
Apart from craters (pores), nodules, cracks, and circular flower-like nodular structures as the main elements forming the surface morphology, anatase nanoparticles sticking on the surface are also visible (Figure 3a).

The change in surface morphology is also reflected in the surface roughness and the corresponding height parameters (ISO 25178), which are increasing with increasing anatase concentration in the electrolyte until $20\,g\,L^{-1}$ addition (**Figure 4**). At $30\,g\,L^{-1}$, the large overlapping number of circular structures results already in flattening effects and roughness is slightly decreasing. However, the surface composition is not affected too much by the anatase addition (**Table 2**), which is understandable from the point of view that only a different polymorph of
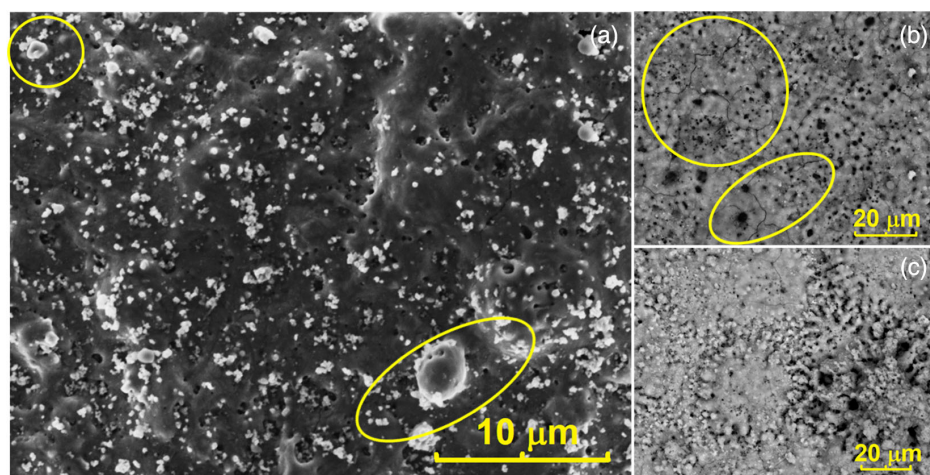
Figure 3. Typical surface morphologies: a) nodular structures and visible anatase particles—$30\,g\,L^{-1}$ anatase sample; b) cracks—$20\,g\,L^{-1}$ anatase sample; and c) flower-like nodules—$30\,g\,L^{-1}$ anatase sample.

**ADVANCED
SCIENCE NEWS**
www.advancedsciencenews.com

**ADVANCED
ENGINEERING
MATERIALS**
www.aem-journal.com

Figure 4. Surface morphology as measured by laser scanning microscope and corresponding height parameters S_z and S_a after 10 min PEO processing as a function of anatase content in the electrolyte.

Table 2. Surface concentration (EDS) of the main elements forming the coating as a function of anatase concentration.

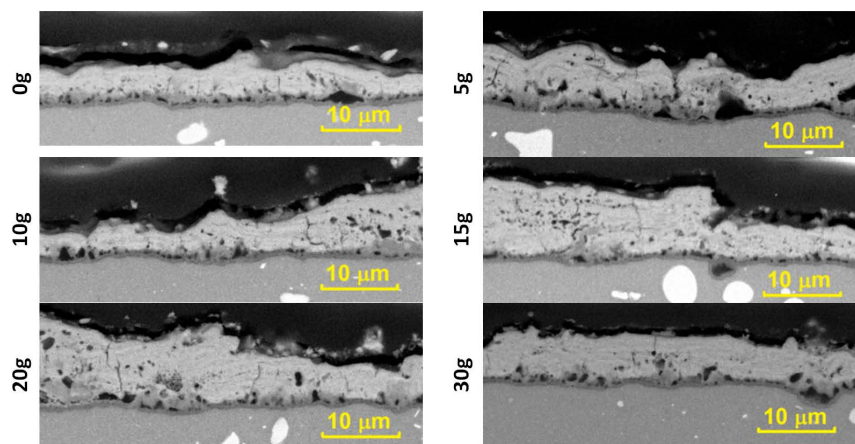| Anatase addition [g L^{-1}]	Carbon [at%]	Oxygen [at%]	Aluminum [at%]	Potassium [at%]	Titanium [at%]	Copper [at%]
0	4.69 ± 0.15	54.96 ± 0.47	2.34 ± 0.91	1.49 ± 0.14	36.33 ± 0.29	0.19 ± 0.02
5	4.49 ± 0.33	54.84 ± 0.39	2.01 ± 0.45	1.87 ± 0.08	36.62 ± 0.41	0.17 ± 0.01
10	4.88 ± 0.32	54.11 ± 1.15	2.57 ± 1.52	1.96 ± 0.04	36.28 ± 0.56	0.20 ± 0.04
15	4.17 ± 0.24	55.03 ± 0.21	1.22 ± 0.14	2.17 ± 0.03	37.26 ± 0.22	0.15 ± 0.02
20	3.96 ± 0.06	55.37 ± 0.23	1.08 ± 0.13	2.16 ± 0.04	35.86 ± 3.44	0.15 ± 0.01
30	4.31 ± 0.16	54.93 ± 0.24	1.19 ± 0.15	1.96 ± 0.07	37.44 ± 0.34	0.17 ± 0.01

TiO_2 is added. However, the values reflect some information from the interface region if the top layer is penetrated by the electrons. Interface and/or substrate are obviously more influenced at lower particle concentrations up to $10\,g\,L^{-1}$. However, the results may suggest that also the outer layer is not fully pure TiO_2.

2.3. Cross Sections, Elemental Distribution, and Coating Thickness

The cross sections of the coatings are shown in **Figure 5**. According to the contrast in the backscattered electrons (BSE) micrographs, the coating consists of three layers with different composition. The lighter the contrast, the heavier the coating forming elements are which is consistent with a higher Ti concentration in the outer layer, the formation of a mixed oxide layer

($TiAl_2O_5$) and an Al_2O_3 barrier layer at the interface between coating and substrate.[34] The coating thickness is not uniform and uniformity is reduced with increasing anatase content in the electrolyte. The interface region consisting of Al_2O_3 and $TiAl_2O_5$ is relatively uniform but wavy. The thickness appears to be independent from the electrolyte composition, showing an average thickness of around 2 μm. Locally, the interface region can be disturbed by strong discharges and the mixed oxide extends outward, toward the surface (indicated by arrows in **Figure 6**, but also visible in all micrographs of Figure 5).

Another feature visible in the coating cross sections is related to the faster dissolution of intermetallics in contact with the electrolyte, resulting in a faster inward growth of the coating filling up fully the dissolved region (Figure 6). The outer layer itself has a minimum thickness of around 5 μm, but can extent locally to around 10 μm. The strong variation of the thickness seems to be

ADVANCED
SCIENCE NEWS
www.advancedsciencenews.com

ADVANCED
ENGINEERING
**MATERIALS**
www.aem-journal.com

Figure 5. Cross sections (SEM-BSE) of PEO coatings with different anatase addition.

related to the observed flower-like structures seen in the surface morphology. The edges of the flowers are supposed to be thicker than the center regions, resulting in nonuniformity of the coating thickness especially with increasing anatase content in the electrolyte.
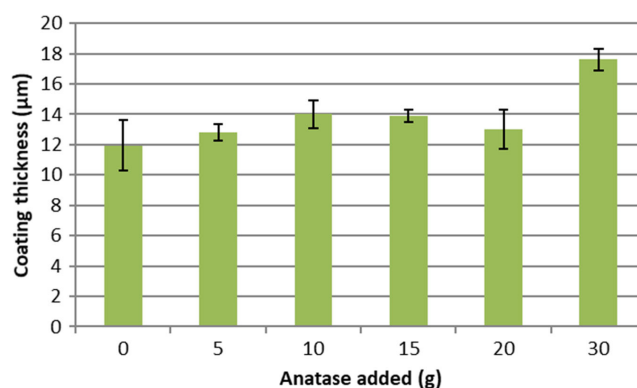
The thickness seen in the cross sections is in average much lower than the values determined by the thickness gauge (**Figure 7**). Considering the size of the gauge and the surface morphology, it is obvious that the gauge is not registering the thinner valley regions as it sits on the hilly regions. Thus, it is recording more or less the maximum thickness values of the coatings.

Those average maximum thicknesses of the coatings formed with different concentrations of anatase particles in the electrolyte are shown in Figure 7. All the coatings have a thickness in the range of 10–15 μm, except for the 30 g anatase specimen whose average thickness is ≈17 μm. It seems as if the thickness is more or less independent from the particle concentration up to 20 g L^{-1}. A further increase seems to stimulate the growth a bit and is related also to the change in surface morphology. However, too high concentration of anatase particles (40 g L^{-1}) caused instabilities in the PEO process and no stable coating formation was obtained anymore.
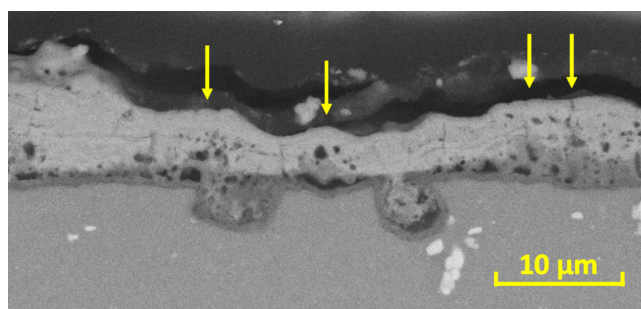
The results obtained by GDOES show that four main regions are found in the depth profiles of the coated specimens, which are defined by the change in slope in the depth profile of Ti, O, Al, and Cu signals, as shown in **Figure 8**. However, important differences are visible by direct comparison of the main coating forming elements Ti, Al, and O (**Figure 9**). Zone I corresponds to the outer PEO layer and it has only titanium and oxygen signals. It implies that the layer has been formed mostly by compounds from the electrolyte during the PEO process. This layer is followed by a region of mixed Ti and Al oxides (zone II), thus a mixture of the materials which are coming from the solution (Ti) and substrate (Al). This zone can be characterized by gradual decreasing and increasing of the titanium and aluminum signals, correspondingly. Figure 9 clearly shows that the zone II is becoming wider after addition of the anatase particles in the solution. For the 30 g L^{-1} anatase addition, there is almost no pure TiO$_2$ on the surface and the mixed oxide (zone II) is dominating. It might be a result of more intense discharges, which contribute to a local expansion of the mixed oxide region (Figure 6, 9, and 10). In the following transition region (zone III), increase in Al signal intensity can be noted, while the Ti signal intensity decreases and almost reaches background level at the end of this zone. The transition region is not sharp, and
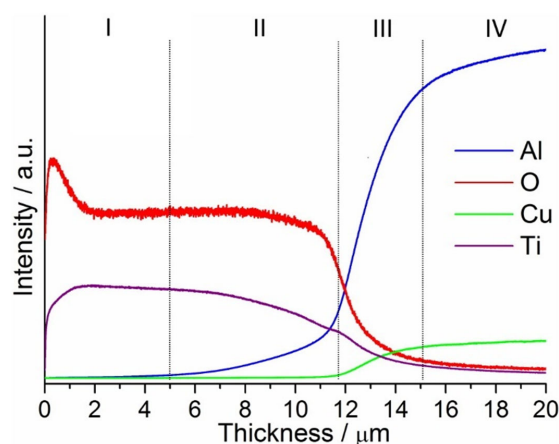

Figure 6. Microstructure (SEM-BSE) of PEO coating without anatase addition to demonstrate two typical features of all coatings. Faster localized inward coating growth in place of dissolved intermetallics and arrows indicate disturbance of the interface layer and extended mixed oxide region by stronger discharges.

Figure 7. Coating thickness as function of anatase concentration in electrolyte (0 till 30 g L^{-1}) measured by thickness gauge.

**ADVANCED
SCIENCE NEWS**

www.advancedsciencenews.com

**ADVANCED
ENGINEERING
MATERIALS**

www.aem-journal.com

Figure 8. Typical qualitative GDOES-depth profile of PEO-coated AA2024 without particle addition.

the PEO layer and substrate alloy are sputtered at the same time. It happens due to the inhomogeneity of the PEO layer thickness (Figure 6). Zone IV represents the substrate and is characterized by high, constant levels of base alloy elements, such as aluminum and copper, while titanium and oxygen have background-level intensity.

Regions of stronger discharges visible in cross sections taken from specimens treated in the standard electrolyte and in $30 \, \text{g L}^{-1}$ anatase addition were also studied by energy dispersive X-ray spectroscopy (EDS) elemental mapping (Figure 10). They confirm that there is stronger mix of the oxide layers in the regions of the discharge, suggesting that substrate, Al_2O_3, and/or mixed oxide material is transported by the discharges toward the surface. However, although those features are visible throughout all treatments, it seems as if stronger discharges are intensified by the presence of particles and are also stimulated by their concentration.

2.4. Phase Composition

The XRD results of all PEO specimens produced with different amounts of anatase particles in the base electrolyte are shown in **Figure 11** and in addition for the standard solution and for the $30 \, \text{g L}^{-1}$ anatase addition measured for three different incident angles in **Figure 12**.
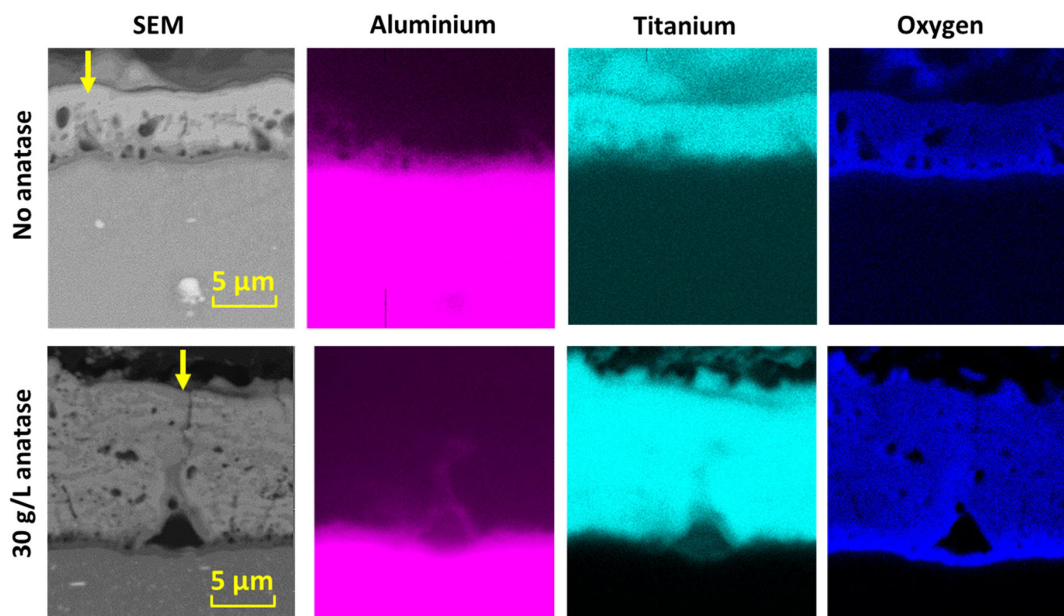
The results indicate that the coating is mainly composed of rutile and anatase. The Al peaks are present because the X-rays penetrate the coating and reach the substrate especially at the higher incident angle of 10°. The coatings seem to have a third phase, which should be the mixed oxide Al_2TiO_5, formed between TiO_2 and Al_2O_3 close to the interface between coating and substrate. In a previous study, it was clearly identified by nanofocused high energy XRD,[34] but here it is only a small low intensity pattern, which is hardly visible only at 10° incident angle. The ratio of anatase-to-rutile can be somehow controlled by the anatase addition. The qualitative results from three different incident angles are shown in Figure 12. At the lowest incident angle (1°) they reflect more the ratio on the surface, at 3° in the center of the coating and at 10° in the full coating volume including the interface region towards the substrate. The results
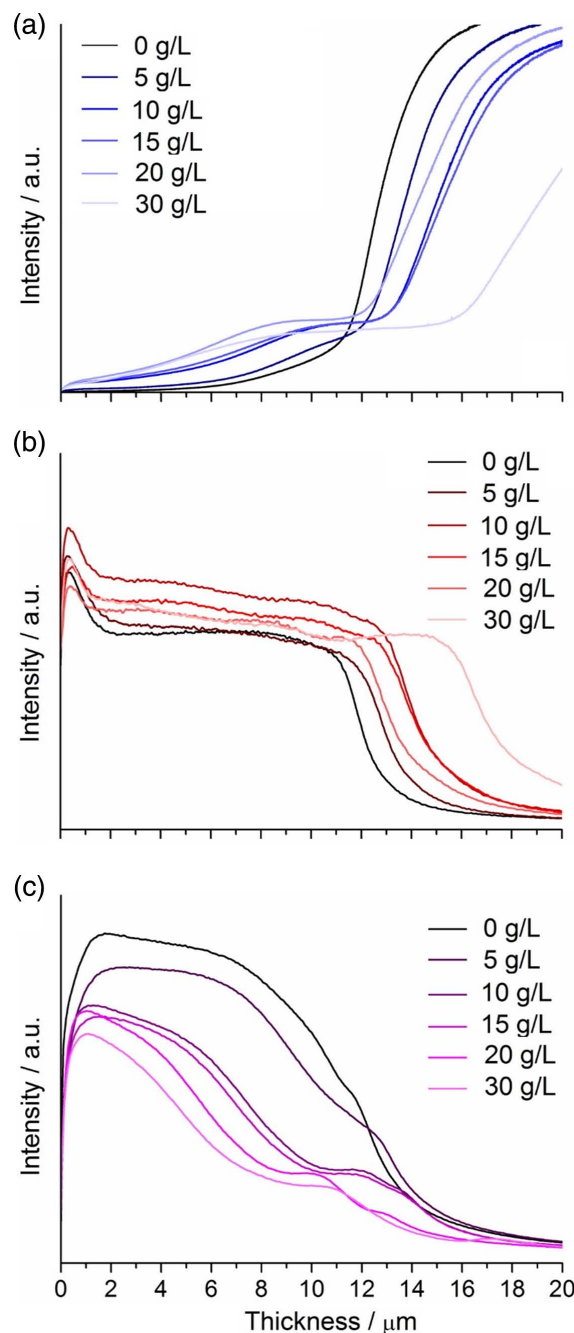
Figure 9. Qualitative GDOES-depth profiles of the main coating forming elements: a) Al; b) O; and c) Ti obtained from the PEO-coated AA2024 prepared in electrolytes with different amounts of anatase particles addition.

indicate that there is a positive effect on the amount of anatase present in the coating if additional anatase is offered via particle addition to the electrolyte (**Figure 13**). Without particle addition, the rutile concentration is two to three times higher than the anatase concentration in the coating. Already with the addition of $5 \, \text{g L}^{-1}$ of anatase particles, the interface concentration of anatase is in the same range as the rutile concentration. The concentration of anatase at the surface and in the middle of the coatings

ADVANCED
SCIENCE NEWS
www.advancedsciencenews.com

ADVANCED
ENGINEERING
MATERIALS
www.aem-journal.com

Figure 10. EDS elemental mapping of a coating region with strong discharges—a) base electrolyte and b) 30 g L^{-1} anatase (the locations of strong discharge are marked with an arrow in the SEM micrograph).
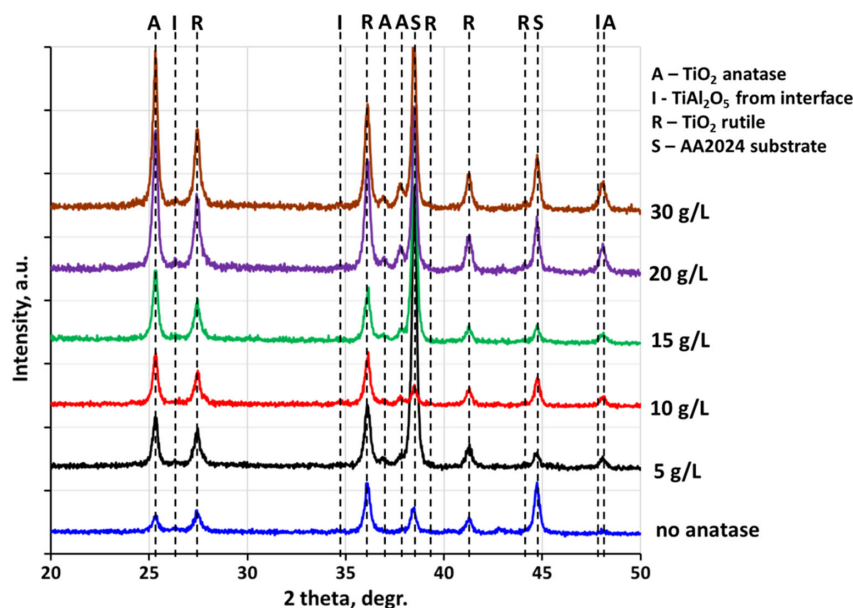
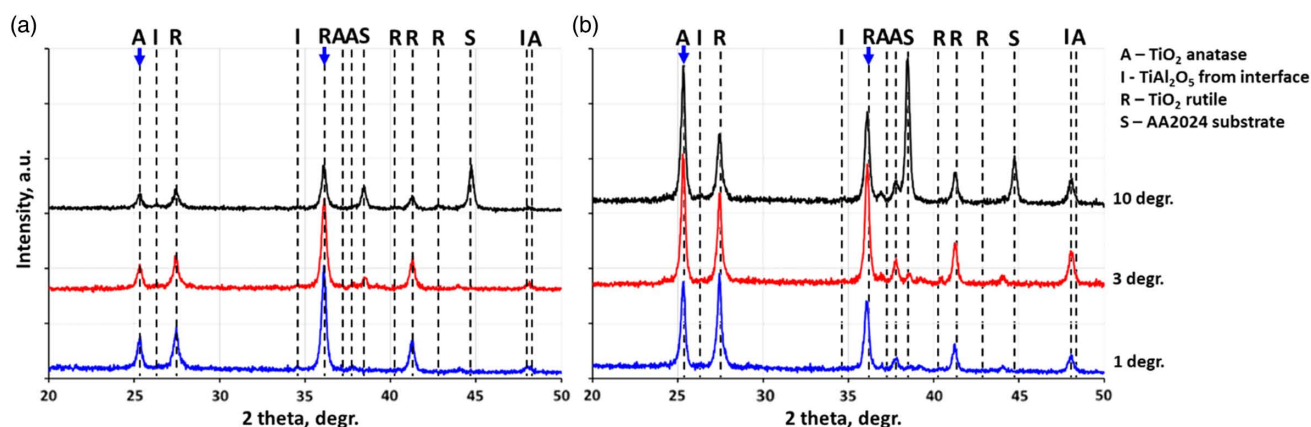**Figure 11.** XRD patterns (10° incident angle) of PEO coatings with 0–30 g L^{-1} anatase particles addition—10 min treatment time.

seems to be always lower. This is most likely related to the uptake mechanisms of the particles, which can enter the coating via open pore fast-track pathways and reach the interface region. Interestingly, anatase concentrations for all three locations are increasing until 15 g L^{-1} and in the center and at the surface of the coating the rutile and anatase concentrations are the same for the first time (ratio is 1). At the interface, the anatase concentration is already higher with a ratio of 0.75. Afterward, they stay quite stable regardless of the anatase concentration in the electrolyte. There is obviously a saturation or equilibrium, which

might be related to competing mechanisms of transport of particles to the coating and their decomposition to rutile by the high energy discharges.

More locally resolved information about the distribution of the phases in the coating and substrate is obtained by scanning a surface area using nanofocused high energy XRD (**Figure 14**). For the standard electrolyte, it is quite obvious that rutile is the dominating phase and that the mixed oxide region appears as a quite well-defined separation between coating and substrate. With the particle addition, the distribution of rutile and anatase

**ADVANCED
SCIENCE NEWS**

www.advancedsciencenews.com

**ADVANCED
ENGINEERING
MATERIALS**

www.aem-journal.com

Figure 12. XRD patterns obtained at three different incident angles—a) standard electrolyte (0 g L^{-1}) and b) 30 g L^{-1} anatase addition. Arrows are marking the rutile and anatase peaks used for calculating the rutile/anatase ratio.
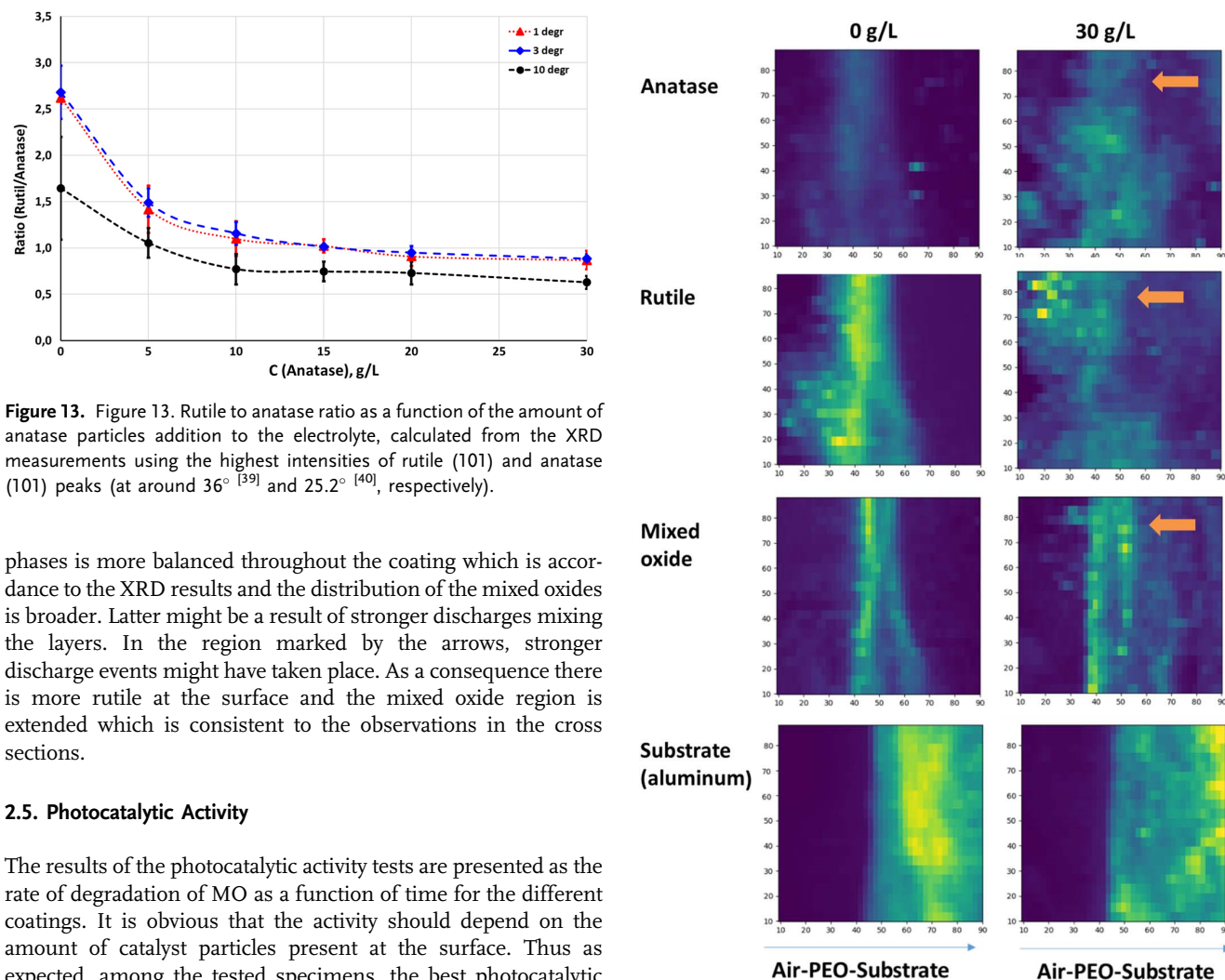
Figure 13. Figure 13. Rutile to anatase ratio as a function of the amount of anatase particles addition to the electrolyte, calculated from the XRD measurements using the highest intensities of rutile (101) and anatase (101) peaks (at around 36° [39] and 25.2° [40], respectively).

phases is more balanced throughout the coating which is accordance to the XRD results and the distribution of the mixed oxides is broader. Latter might be a result of stronger discharges mixing the layers. In the region marked by the arrows, stronger discharge events might have taken place. As a consequence there is more rutile at the surface and the mixed oxide region is extended which is consistent to the observations in the cross sections.

2.5. Photocatalytic Activity

The results of the photocatalytic activity tests are presented as the rate of degradation of MO as a function of time for the different coatings. It is obvious that the activity should depend on the amount of catalyst particles present at the surface. Thus as expected, among the tested specimens, the best photocatalytic activity was demonstrated by the sample that was subjected to PEO with 30 g L^{-1} of anatase particles addition, showing that 31.6% of total MO was degraded. The sample that underwent PEO process with 20 g L^{-1} of anatase particles was able to

Figure 14. Distribution of the main phases in the coating and near substrate region determined by nanofocused high energy XRD. The orange arrow marks regions, where stronger discharge events appear to have taken place.
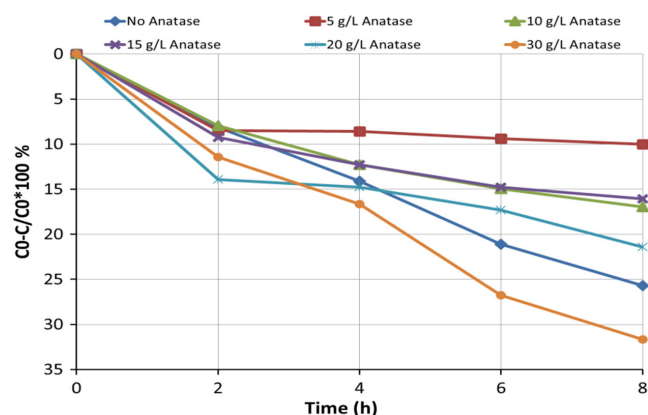
Figure 15. MO degradation as a function of time.

degrade 21.4% of MO after 8 h, while the 10 and 15 g L^{-1} anatase specimens decomposed 16–17% of MO and the 5 g L^{-1} anatase specimen demonstrated the worst photocatalytic activity degrading only 10% of initial MO. All results obtained for 2, 4, 6, and 8 h are shown in **Figure 15**. Interestingly, the base electrolyte sample was able to degrade 25.7% of total MO introduced, although the surface concentration of anatase was the lowest.

Despite the unexpected good performance of the standard specimen, the addition of anatase particles to the electrolyte seems to have a clear positive effect on the photocatalytic activity. It mainly depends on how much anatase is incorporated into the surface and the surface roughness determining the surface area available for the decomposition reaction. Considering the surface morphology, there seems to be a change in the incorporation mechanism starting with a concentration of 20 g L^{-1}, when more flower-like circles appear. At 30 g L^{-1} when almost the full surface is covered by them, the effective surface area seems to be the highest. Although having a similar anatase concentration at the surface, the increasing surface roughness related to the

flower-like structure may contribute to the better performance with increasing particle concentration in the treatment electrolyte.

2.6. Wear Properties

The wear tests were performed with increasing loads to identify the load bearing capacity of the coatings. **Figure 16** shows the changes in the friction coefficient (f_c) as a function sliding distance for the highest load for each coating before the coating fails.
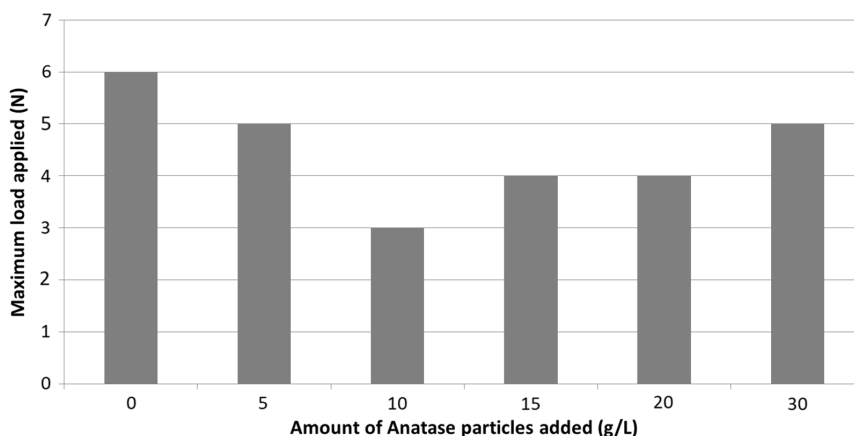
The values of f_c exhibit a continuous increase independently of the load applied, until they reach a constant plateau region. The graphs show that f_c is rather low (less than 0.2) at the start of the tests, and then have a relatively quick increase to the 0.7–0.8 range. This is related to the running in of the wear process where the coating/ball contact area is increasing, which is finished after around 500 s (2.5 m). At lower loads the specimen surface is not fully flattened and the contact area is smaller compared with higher loads, thus at 3 N the f_c is 0.6, while at the higher loads it reaches almost 0.8. There is no influence of the particle addition on the f_c visible. A friction coefficient of 0.4–0.5 indicates the failure of the coating and direct steel/aluminium contact. Only one example (10 g L^{-1} anatase –4 N) is shown for the coating failure (Figure 16).

Adding anatase particles does not affect the friction coefficient values (Figure 16), but changes the load bearing capacity (**Figure 17**). Latter shows a drop from 6 N (no particles) down to 5 N if 5 g L^{-1} particles are added. With further increasing amount of particles (10 g L^{-1}), the load bearing capacity drops down to 3 N before it is stabilized and starts to increase again to 4 N for the 15 and 20 g L^{-1} samples. The 30 g L^{-1} anatase specimen showed the highest thickness, but it was not able to endure loads higher than 5 N.

Figure 18 and **19** show images of the wear tracks formed on the coated samples that were subjected to different loads. Figure 18 shows examples of wear tracks formed on specimens
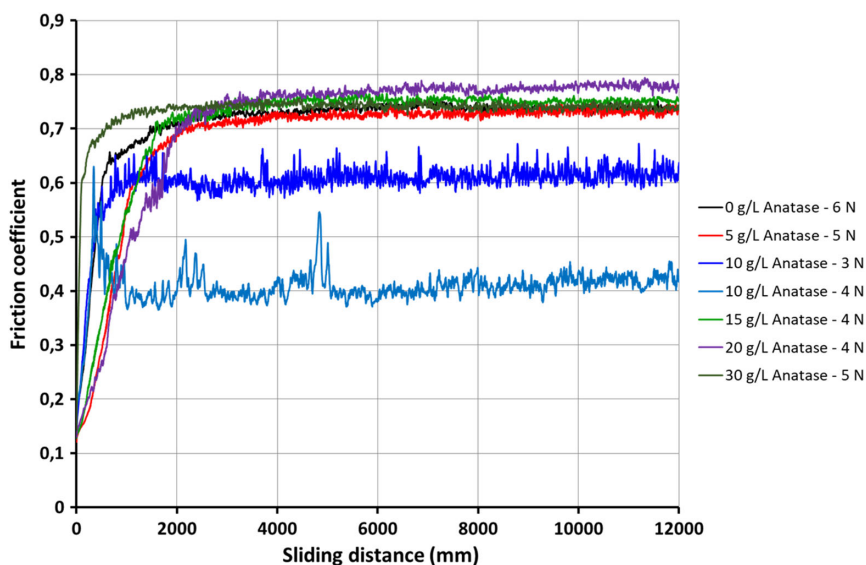

Figure 16. Friction coefficient as a function of sliding distance for specimens without and with different amounts of anatase particles.

ADVANCED
SCIENCE NEWS

www.advancedsciencenews.com

ADVANCED
ENGINEERING
MATERIALS

www.aem-journal.com

Figure 17. Comparison of maximum loads applied in the wear tests of specimens without and with anatase, without coating failure.
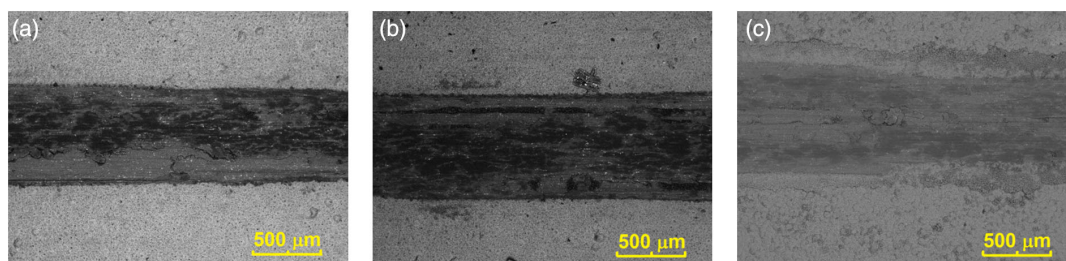
Figure 18. Wear tracks on samples that failed the wear test under different loads applied: a) $10 \, g \, L^{-1}$ anatase—4 N; b) $15 \, g \, L^{-1}$ anatase—5 N; and c) $30 \, g \, L^{-1}$ anatase—6 N.
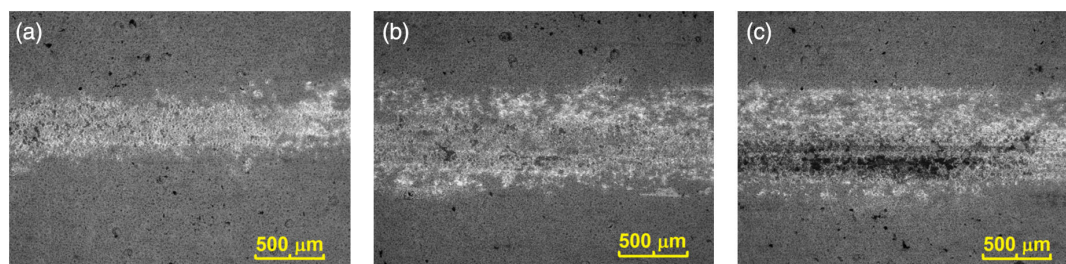
Figure 19. Wear tracks on samples that passed the wear test under different loads applied: a) $10 \, g \, L^{-1}$ anatase—3 N; b) $15 \, g \, L^{-1}$ anatase—4 N; and c) $20 \, g \, L^{-1}$ anatase—5 N.
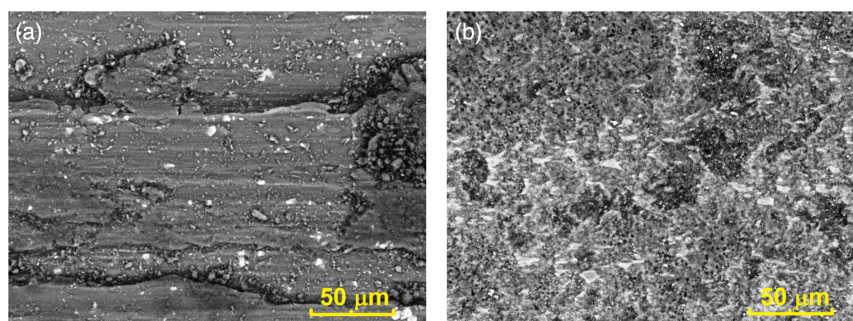
that could not withstand the applied load, while Figure 19 shows those wear tracks on coatings, which survived the applied load.

As expected, the average width of the wear tracks seems to increase with increasing applied load. This can be explained by the fact that the ball and specimen suffered wear and increased the area of contact between them with increasing applied load.

The images in Figure 18 and 21b show the complete removal of the coating along the wear track leaving the substrate exposed to the steel ball, where it experiences a considerable damage by abrasion and adhesion. The substrate shows signs of severe plastic deformation in combination with abrasive wear. The debris from the coating and from the ball acts as third body and the

hard particles cause abrasive wear as they plough through the soft substrate under the movement of the ball (**Figure 20**a). In **Figure 21**b, clear transfer of substrate material toward the ball is visible, indicating also adhesive wear. In the cases when the coating has sufficient load bearing capacity, there is almost no wear of the coating and mainly debris from the ball is visible on the specimen surface (Figure 20b and 21a).

In summary, the coating that showed the best tribological behavior was the one without particle addition, although it exhibited the lowest thickness. This demonstrates that the particle addition is detrimental for the wear resistance, probably because of some embrittlement of the coating due to the particles as well as loose particles acting as hard third body components in the

**ADVANCED
SCIENCE NEWS**

www.advancedsciencenews.com

**ADVANCED
ENGINEERING
MATERIALS**

www.aem-journal.com

Figure 20. Cases of the PEO coating being a) completely removed and the substrate becoming exposed: 20 g L^{-1} anatase—5 N; and b) the coating remaining adherent leaving the substrate partially exposed: 15 g L^{-1} anatase—4 N.
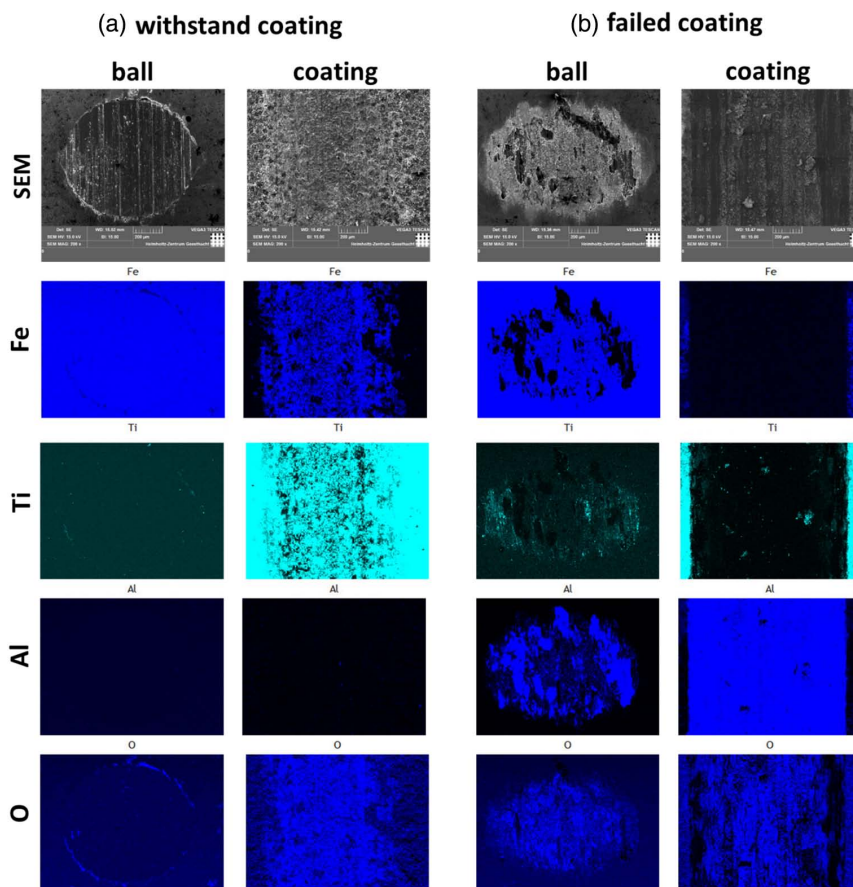
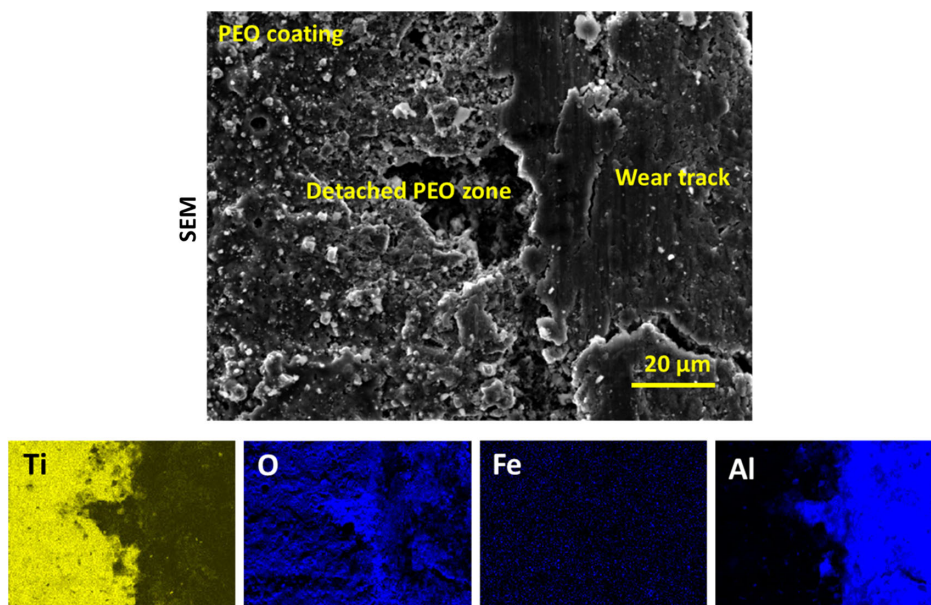

Figure 21. Elemental distribution maps after the wear test in the case of withstand and failed coatings. PEO treatment in the presence of 15 g L^{-1} anatase is selected as representative.

wear process. Among the particle additions, the thickest coating formed with the highest amount of particle addition performed the best, but still failed at a 2 N lower load compared with the coating without particles. All coatings with particles that were subjected to loads higher than 5 N were removed completely by abrasion caused by the steel ball. The failure seems to appear in two steps. In the first step, the coatings are pressed into the substrates and the brittle coatings are not able to follow this plastic deformation and start to crack. In the second step, small bits

of the coatings are losing the adhesion to the substrate. **Figure 22** shows this mechanism in more detail. At the edge of the wear track, a bit of the coating is removed by flaking-off due to the generated stresses and deformations leaving behind the uncovered substrate. Afterward, they are either removed from the wear track or even worse are stay and contribute as third body in the wear process between the steel ball and AA2024 substrate. Nevertheless, the coating represents an effective way to increase the wear resistance of aluminum alloys, considering that the rate

**ADVANCED
SCIENCE NEWS**

www.advancedsciencenews.com

**ADVANCED
ENGINEERING
MATERIALS**

www.aem-journal.com

Figure 22. Elemental distribution maps after the wear test in the case of failed coating, demonstrating the character of coating damage (6 N load). PEO treatment in the presence of $15\,g\,L^{-1}$ anatase is selected as representative.

of material removal is significantly lower than that obtained for the bare aluminum alloys subjected to the similar test.

2.7. Degradation Behavior

The specimens after 336 h of immersion in 3.5% NaCl solution are shown in **Figure 23**. There are no severe corrosion marks visible on the surface, which is as expected from previous corrosion studies of the coatings.[34] However, there are some darker marks on the coating without particle addition, which may indicate local failure of the coating and substrate appearance. Note that the corrosion products on the bare alloy are also darker and have a similar appearance (Figure 23g). In contrast, there are also white localized corrosion products on the 10 and $30\,g\,L^{-1}$ anatase specimens which might be related to a localized dissolution of the coating or some redeposition of corrosion products from the nonprotected region of the electrical contact point of the PEO process. Further characterization of the surfaces by XRD after the immersion does not show the appearance of a detectable amount of corrosion products on the surface nor the dissolution

of major coating phases for the specimen with particle addition (**Figure 24**). However, the specimen treated in the standard electrolyte without particle addition seems to fail partly and Al_2O_3 either formed as corrosion product or coming from the barrier layer can be detected. Latter means that the top TiO_2 top layer was partly removed.

3. Discussion

The PEO process is recognized as an environmentally friendly technology and offers a wide range of possible applications while producing thick, hard, and well-adhered ceramic type of coatings. The PEO technique has been used to modify the surface of a light metal alloys using microarc formation on the workpiece under immersed conditions in a temperature-controlled aqueous electrolyte.[12–14,35] The process parameters such as electrolyte composition, temperature, additive addition, current density, voltage, treatment time, and so on offer the opportunity to tune the PEO process and obtain coatings of different porosity and properties. Due to the porosity, the coatings can be impregnated
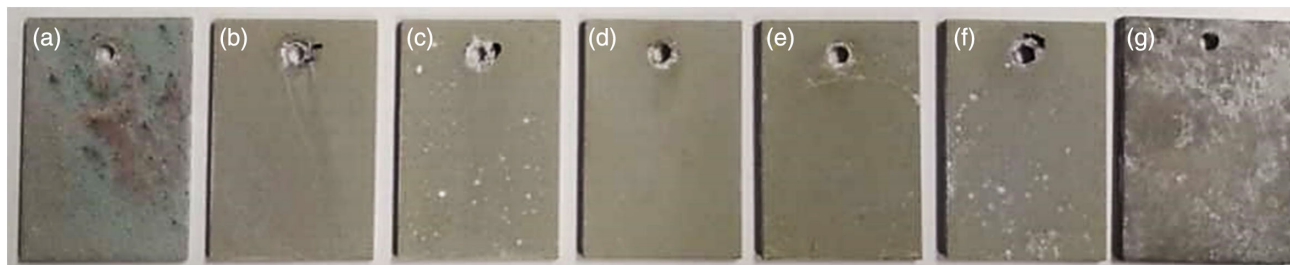
Figure 23. The surface view of the samples after 2 weeks of immersion in 3.5 wt% NaCl electrolyte with following additives of anatase particles in PEO electrolyte: a) $0\,g\,L^{-1}$, b) $5\,g\,L^{-1}$, c) $10\,g\,L^{-1}$, d) $15\,g\,L^{-1}$, e) $20\,g\,L^{-1}$, f) $30\,g\,L^{-1}$, and g) not coated material.
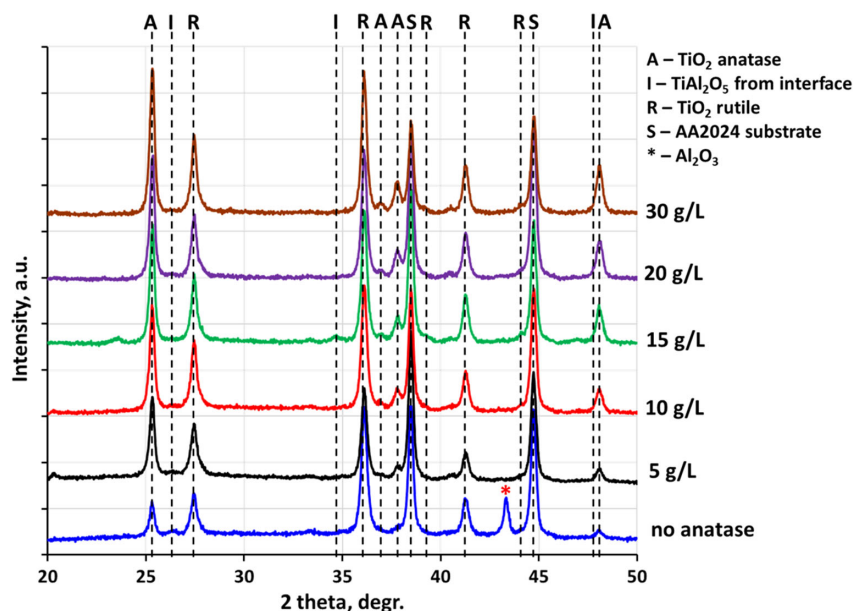
Figure 24. XRD patterns (10° incident angle) of PEO coatings with 0–30 g L^{-1} anatase particles addition (10 min treatment time) after 2 weeks of immersion in 3.5 wt% NaCl electrolyte.

with catalytic particles (e.g., TiO$_2$), which will create new applications in the field of environmental protection. This impregnation concept was proved, but also a couple of problems were identified which limits the successful application of PEO processing to form photoactive surfaces, which will be discussed in the following.

Surprisingly, the PEO films formed on Al alloy in potassium titanium oxide oxalate dihydrate solution were mainly composed of TiO$_2$ (Figure 11 and 12). Rutile is the main phase of the coatings, but it can be shifted toward the direction of anatase by a direct incorporation of anatase nanoparticles from the electrolyte (Figure 13). From the cross sections and elemental mappings, it is visible that the coating structure is more complex. Only the top layer is composed out of TiO$_2$, followed by a region of mixed oxides (Al$_2$TiO$_5$) and a thin interface layer, which is most likely pure Al$_2$O$_3$. The thickness of latter is far less than 0.5 μm, and thus it is difficult to identify it as a phase by the diffraction techniques. However, the assumption is based on intensity differences in the EDS elemental mappings (Figure 10) and mainly on the BSE contrast in the SEM cross sections (Figure 5).

The addition of anatase particles at lower concentrations in electrolyte does not affect the coating thickness significantly (Figure 7); however at 30 g L^{-1}, the coating becomes slightly thicker at the same processing time. However, with increasing amounts of anatase particles added to the electrolyte, the surface morphologies are changing (Figure 2), with the biggest change between 20 and 30 g L^{-1}. Five different features determine the surface morphology (Figure 3)—pores, craters, cracks, nodules, and anatase particles partly incorporated into the surface. Pores are formed due to melting and resolidification of the surface under the discharges and incorporation of gas bubbles, which are generated in the process. There are at least two different types of discharges. There are the classical discharges across the coating, which are responsible for the crater-like structures, which

are formed by ejected molted material through the discharge channels (due to the high melting temperatures of the involved phases, the volume is quite low). The number of these pores and their density decrease with anatase particle addition, but they grow in size. Thus, the intensity of a single discharge or local discharge event across the coating is obviously increasing due to the particle addition. However, with higher anatase concentration not only the intensity of the standard discharges is increasing, but also the second discharge mechanism becomes more dominant, which seems to be responsible for particles melting and sintering together and forms flower-like circular structures (Figure 3c). Those flower-like structures are associated with intense surface discharges forming preferentially at the triple interface of gas bubbles, electrolyte, and coating. They contribute to sealing or covering of the classical pores so that almost no open surface pores can be observed for the 30 g L^{-1} sample. However, both discharges can combine at one location; the partly sealed surface is responsible that the classical type of discharges occur less frequently but with much higher energy and therefore generate more melt volume and mixing of the phases. This is visible in the GDOES-depth profiles in form of the increasing mixed oxide region (zone 2) in Figure 8 and 9. However, the extension of the mixed oxide zone is not uniform, but occurs locally restricted depending on the high energy discharge events. This stronger mixing is clearly visible not only in the cross sections (Figure 5, 6, and 10), but also on the surface (Figure 2d,f). Furthermore, the area of stronger mixing by more intense discharges can also be correlated to regions containing more rutile compared with anatase (Figure 14).

The XRD results reveal the crystalline nature and the phases of the PEO coatings (Figure 11–13) and the intensity of the diffraction peaks can be used to estimate the rutile to anatase ratio. Surprisingly, the anatase/rutil ratio in the coating reaches already at around 15 g L^{-1} anatase particle addition in the electrolyte its

maximum and further increase of the anatase electrolyte concentration does not change it much anymore. One of the reasons can be the polymorphic transformation of anatase into rutile at higher temperatures[36,37] and/or limited transport capacity through the open pores (especially if the change in the dominant discharge mechanism is stimulated by increasing amount of particles and contributes to sealing of the open porosity). The ones, which are trapped in the melt pools at the surface, are converted to rutile by the discharges. The result is a kind of equilibrium condition between anatase and rutile fraction. At higher anatase concentration, more new anatase is available, but also more anatase is converted to rutile due to the more intense discharges. The chance for anatase to survive seems to be higher close to the interface where the particles, which were entering by the open pores, are stored in the remaining open porosity. The rutile to anatase ratio is the lowest when the X-rays penetrate deeper and reach the interface region. Close to the surface and in the center of the coatings, the ratio is higher (Figure 13).

The GDOES-depth profiles reveal the existence of four zones in the depth profile of the PEO coatings. Zone I represents the surface layer, which is rich in Ti and O (Figure 8). The presence of Ti indicates that it has been incorporated from the electrolyte during the PEO process, as the charged TiO complexes $[TiO(C_2O_4)_2]^{2-}$ are decomposed under the discharges conditions

and form TiO_2. In addition, the results confirm that higher amounts of anatase particles added to the electrolyte do not significantly contribute to increasing the coating thickness, except in the case of 30 g L^{-1} anatase. There is a region (Zone II) where both oxides (TiO_2 and Al_2O_3) do appear at the same time. Mixed oxide with the stoichiometry according to $TiAl_2O_5$ was identified by the XRD studies (Figure 11 and 12). With increasing particle concentration, the zone II is growing on expense of zone I and obviously reaching the surface at 30 g L^{-1}, suggesting that pure TiO_2 is not existing anymore. However, this is not the case as the mixed oxide zones, which reach the surface, are related to strong discharge events which are locally restricted islands in a matrix of TiO_2. Zone III is the interface region (most likely a pure Al_2O_3 layer), which cannot be resolved because of its low thickness and the waviness of the interface. Finally, the substrate is reached (zone IV) which is indicated by the presence of only Al and the other alloying elements.

Summarizing the above, one can suggest a coating formation process that depends on the particle concentration in the electrolyte (**Figure 25**). Interestingly, in contrast to many standard PEO processes in which compounds (often oxides) or mixed compounds (oxides) of the substrate and electrolyte are forming, the top coat contains mainly TiO_2 a compound which is formed solely from the electrolyte. The process starts similar regardless
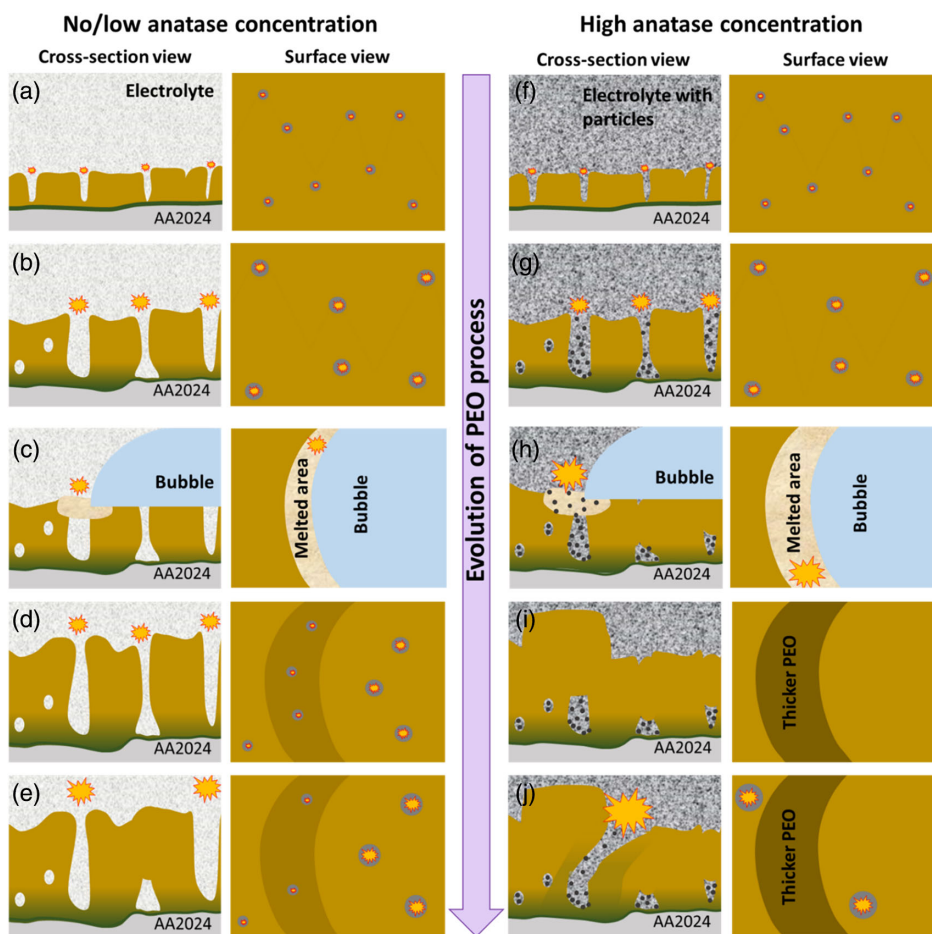
Figure 25. Evolution of PEO process and influence of the particle concentration.

of the particle concentration (Figure 25a,f) with an anodization process, which forms an Al_2O_3 barrier layer. If the breakdown voltage of the barrier layer is exceeded, a large number of low intensity discharges are forming. Obviously, the charged TiO complexes $[TiO(C_2O_4)_2]^{2-}$ are attracted toward the surface and decomposed under the discharge conditions and form TiO_2. The layer growth in the following sequence (Figure 25b,g) is based on this decomposition driven by discharges mainly across the top TiO_2 layer with only a small amount of mixing between TiO_2 and Al_2O_3. As the thickness of the top oxide layer is increasing, the size of discharge channels (open pores) is increasing due to the higher energy required to drive the discharge. With increasing size, more anatase particles can enter and reach the interface region where kinds of anatase reservoirs in the open pore structure are formed. This uptake depends strongly on the concentration and size of particles in the electrolyte (Figure 25g). However, if the energy of the discharge reaches a certain limit, also a second discharge mechanism starts, which is related to gas bubbles sticking on the surface. At the triple interface coating/electrolyte/gas, the electrical field is strong and discharges are generated all along the interface (Figure 25c,h) forming circular melt pools with the bubble in the center. In the electrolyte with no or low particle concentration, the electrolyte is less viscos and bubbles are sticking less frequently and for shorter periods at the surface. Thus, the number and intensity of those circular discharge events is less. As consequence, the melt pools are smaller compared with electrolytes with high particle concentration (Figure 25d,i). Furthermore, less particles are available, which can stick to the melt pools where they are melted and/or sintered together. Overall, for the low concentrated electrolytes the number of circular discharge events and the volumes in the formed circular melt pools is not enough to seal the open porosity of the PEO coating and the PEO process continues with discharges across the interface/coating (Figure 25e). With further increase in the thickness, the intensity of the discharges is increasing, causing an increasing intermixing of the oxides in the discharge region, but do not reach the surface (Figure 25f). In contrast, in electrolytes with high concentration of particles, the circular events are more frequent and of longer duration, thus the melt pools are larger. As a consequence, more particles which are also available in higher number in the electrolyte are captured in the melt pools and/or are sintered together by the discharges (Figure 25i). The coating in the circular regions around the bubbles is growing much faster covering and/or converting the original porous surface to a dense layer (Figure 25i). Discharges are diminished in this region for a moment. However, with continuation of the processing, the field strength is further increasing and the regions close to the "rings" are weak points and locations for new high intensity discharges. The energy is high enough to melt the Al_2O_3 interface region and TiO_2 of the surrounding coating and to eject the mixed oxides out of the larger discharge channels (Figure 25j).

Contrary to the treatment time, which is not essential when it comes to photocatalytic activity,[34] the addition of anatase particles to the electrolyte seems to be. The photocatalytic activity of the specimens increased when higher amounts of anatase were added, but a certain limit needs to be exceeded. Up to the addition of 15 g L^{-1} anatase, the activity is almost the same. This finding is quite interesting as aforementioned results indicate that the amount of anatase is increasing until 15 g L^{-1}. Obviously, the change in the PEO mechanism involving the circular discharge events changes the surface morphology and with it the roughness which influences positively the active surface area rather than the amount of active phases. Thus, the best results were measured for the sample that was subjected to PEO with 30 g L^{-1} of anatase particles addition, showing that 31.6% of initial concentration of MO was degraded (Figure 15).

The wear tests showed that increasing the concentration of anatase particles (up to 10 g L^{-1}) in the electrolyte has first a negative effect on the wear resistance, but at higher concentration ($\geq$15 g L^{-1}) improvements are observed again, although the performance of the layer without particles is not reached. The improvement might be related to the extended mixed oxide region enhancing the bonding to the substrate or creating harder coating phases. However, the best wear performance was obtained for coatings produced without any particle addition (7 N load bearing capacity; Figure 17). When the PEO coating does not withstand the load, the surface layer gets pressed into the surface, being cracked, and stripped away due to its brittleness and porosity, leaving the substrate exposed, where it endures more plastic deformations and abrasive wear due to the hard small fractions of the coating (Figure 20 and 21). It seems as if particle additions are detrimental because they are not always tightly bonded to the surface and can act as hard third bodies in the wear process leading to earlier failure; furthermore, they are defects in the coating and increase the brittleness and likelihood of earlier cracking.

The degradation studies confirm that the coatings are stable enough to be exposed to more aggressive environments for a longer period without major damage, loss, or change in coating phases if particles were incorporated into the coatings. Without particle addition, the coating is less resistant against a corrosive environment. It seems as if corrosion products are forming in the interface, resulting in a volume increase which generates stresses and results in a flaking-off of the TiO_2 top layer. Thus, the improvements in stability seem to be related to the extended formation of the interface mixed oxide region as a result of more extensive discharges in the presence of particles in the electrolyte. This mixed oxide interface layer is obviously the main barrier layer to prevent direct contact of substrate and electrolyte.

Considering a possible application as coated sheets for photocatalytic wastewater cleaning, the results indicate some problems which still need to be solved. The amount of anatase, which can be transferred to or maintained in the coatings by particle addition, seems to be limited and the highest anatase concentration is not at the surface, but at the interface. The change in discharge mechanism increases the surface roughness, which is considered as a positive effect on the photocatalytic activity, but at the same time it increases the discharge intensity which induces more anatase to rutile conversion and leads to more Al_2O_3 in the surface region which are considered as negative effects. The mechanical robustness and stability in aggressive, water-based solutions are given, but particle addition has also negative effects on the performance compared with a particle-free coating. Furthermore, the overall photoactivity is still quite low and needs further tuning if sunlight should effectively be used.

4. Conclusions

The results of the current study suggest that: 1) TiO_2 coatings can be formed on Al substrates and the anatase concentration can be increased by anatase particle addition. However, an upper limit exits, which seems to be related to blocking of open porosity as fast pathways for particle uptake and anatase to rutile polymorph transformation by high intensity discharges. 2) The coating formation is based on a decomposition mechanism of the electrolyte with the ability to form pure TiO_2 film if no particles are used in the electrolyte. 3) Adding particles influences the discharge mechanisms. At low concentration, a typical discharge mechanism across the oxide surface film is dominant. The coating is characterized by an open surface pore structure. At high concentration, circular discharge events (related to bubbles sticking at the surface) are creating flower-llike surface structures, which seal the open porosity. The coating is characterized by the circular flower-like rings and low number of open pores. 4) Adding particles increases the intensity of the discharges, leading to stronger intermixing between TiO_2 from the surface film and Al_2O_3 from the interface layer. 5) Adding anatase particles can increase the photoactivity of the surface, which is probably more a result of increasing the surface area rather than the amount of anatase. The highest anatase concentration is always at the interface and not at the surface. 6) Mechanical and chemical stability of the films are sufficient.

5. Experimental Section

Material, Electrolyte, and Setup: Samples of AA2024 aluminum alloy (3.8–4.9% Cu, 0.35–0.5% Fe, 0.1% Cr, 1.2–1.8% Mg, 0.3–0.9% Mn, 0.5% Si, 0.1–0.15% Ti, 0.25% Zn, 0.15% others, and Al balance) comprising 30 mm in length, 20 mm in width, and 1.5 mm in thickness were subjected to the PEO treatment. PEO treatments were conducted using a laboratory setup, which consists of a Hameg analogue oscilloscope HM400 40 MHz, a self-made pulse generator, and a 3000 W EA-PS 8720-15 DC power supply. The samples were treated for 10 min in constant current mode applying 50 mA cm^{-2} and a pulse ratio of $t_{on}:t_{off} =$ 1 ms:9 ms. The power supply was designed to allow independent control over the main pulse parameters, such as pulse duration, voltage, and current density. Bubbling and cooling systems kept the electrolyte temperature at 20 ± 0.1 °C and the particle distribution homogenous during the whole process.

For the PEO treatments, the samples were immersed in an aqueous electrolyte solution containing 40 g L^{-1} of potassium titanium oxide oxalate dihydrate and various amounts of anatase particles (Sigma-Aldrich, TiO_2, 99.8% anatase powder, average particle size less than 5 μm) ranging from 5, 10, 15, 20 up to 30 g L^{-1}. The electrolytes used were close to neutral, with their pH values in the range of 6 ± 0.5. The Zeta potential of the TiO_2 particles in titanium oxide oxalate dihydrate aqueous electrolyte was measured for the final solution containing 30 g L^{-1} anatase using a Stabino I system (ParticleMetrix, Meerbusch, Germany). The Zeta potential was recorded every 5 s for 300 s and showed an average value of −9.5 ± 1.2 mV.

Coating Characterization: A scanning electron microscopy (SEM; Tescan VEGA3) was used to observe the surface morphology and perform cross-sectional analysis of the obtained PEO coatings. To prevent the effect of surface charging, PlanoCarbon N650 was applied to cover the resin surface and to contact the specimen prior to analysis.

A thickness gauge (Elektro Physik, MiniTest 2100) was used for non-destructive thickness measurements. A minimum of ten measurements were taken randomly on the surface and the average values were

calculated. The measurements were performed directly after the coatings were rinsed with deionized water and dried under air after the PEO processing.

The phase composition of the coatings was analyzed using X-ray diffraction (XRD) with a Bruker D8 Advance diffractometer. Cu Kα radiation source, equipped with a nickel filter, was used. A step size of 0.02° and scanning rate of 1 s per step in the 2θ range between 20° and 50°, with different incident angles of 1°, 3°, and 10°, were selected as default measurement conditions. With changing incident angle, the penetration depth of the X-rays was changed allowing to collect phase composition information closer from the surface (1°), down to the center of the coating (3°) and from the full coating volume including substrate (10°). To check reproducibility of phase ratio through the coating thickness, XRD measurements were performed at least four times and the average values were calculated. Furthermore, corrosion products were analyzed under an incident angle of 10° after 14 days of immersion in 3.5% NaCl solution.

The phase distribution across the coating was studied at PETRA III (DESY, Hamburg, Germany) at the nanofocus endstation of P03 beamline,[38] with an X-ray energy of 19.8 keV and a beam size of 1.5 μm × 1.5 μm. The phases of the coating and interface regions were investigated by performing a mapping (mesh) scan with a size of 80 per 80 μm with a step size of 2 and 4 μm, in perpendicular and lateral directions, respectively. An Eiger 9M detector (pixel size 75 μm × 75 μm) with an acquisition time of 0.5 s was used. Data treatment and analysis were conducted by a specially designed Python script. This script also was used to plot 2D maps of the distribution of main phases in the coating. The diffraction profiles were normalized to the ionization current in a gas chamber setup in front of the sample along the beam path. That allows to correct X-ray beam intensity variations, making the total scattered intensity directly proportional to the gauge volume.

Laser scanning confocal microscope (LSM 800, ZEISS, Germany) was used to monitor the roughness of the obtained PEO coatings with different amount of anatase addition (magnification ×20 was selected). ConfoMap software was used for subsequent data treatment and analysis. The height parameters (S_z—maximum height of the surface, μm and S_a—arithmetical mean height of the surface, μm) of rough PEO coatings were calculated according to ISO 25178 standard.

The depth profile analysis of the PEO coatings was performed using glow discharge optical emission spectroscopy (GDOES, HORIBA) using a standard 4 mm copper anode with a distance of 0.1 mm from the sample. Argon was used as a plasma gas at an operating pressure of 650 Pa and a power of 30 W. The depth of sputtering was estimated by using sputtering rate coefficient, which was obtained by simple dividing of the coating thickness (obtained by other techniques) by sputtering time.

The photocatalytic activity of all samples was evaluated by following the degradation process of methyl orange (MO).[19] The photocatalytic degradation was conducted in a glass cell, which contained 10 mL aqueous solution of MO (8 mg L^{-1}), under constant stirring conditions (400 rpm) and lighting. In the experiment, the catalyst (sample surface) was positioned on a perforated holder (the same size as the PEO sample and 4 mm high) with a magnetic stirrer below it. The reaction solution was kept at room temperature (25 °C) by surrounding the photocatalytic reactor with a water cooling jacket. Prior to the photocatalytic degradation, the catalyst and solution were stirred for 30 min in the dark to obtain adsorption–desorption equilibrium. The solar radiation was provided by a lamp with 16 000 lux intensity (Osram Vitalux 300 W) vertically placed at 25 cm above the surface of the solution. Aliquots (1 mL) were collected every 2 h during the time span of 8 h, immediately analyzed, and taken back to the initial solution. The MO concentration was determined by measuring the maximum of the absorption spectra at $\lambda_{max} =$ 464 nm. The changes in MO concentration were measured using a Thermo Scientific Evolution 220 spectrophotometer in the range from 250 to 700 nm. Based on a standard curve showing the linear dependence between MO concentration and absorption at 464 nm wavelength, the measured absorption (at $\lambda_{max} =$ 464 nm) was recalculated to concentration. The stability of MO solution was tested under the same conditions as the catalyst. After being exposed to 8 h of irradiation, the initial MO concentration remained unchanged proving its stability. This confirms that the observed

MO degradation is the result of a photocatalyst's presence. The degradation rate of MO was calculated as $((C_0-C)/C_0)$, where C_0 stands for the initial concentration of MO and C stands for the concentration of MO at designated time intervals after irradiation.

The dry sliding wear resistance of PEO layers was assessed with an oscillating wear test device (TRIBO Technic, France). A steel ball with a diameter of 5 mm (100Cr6) as the counterpart and a sliding distance of 12 m at a linear speed of 6 mm s^{-1} was selected. Loads varied from 3 to 7 N depending on the specimen to determine the load level and sliding distance at which the coatings failed. A new steel ball was used for each test.

The long-term stability of the coatings was tested by a simple immersion test in a neutral 3.5% NaCl solution. The surface-to-electrolyte volume ratio was 1:4 cm^{-1} and the total immersion duration was 336 h. Afterward the specimens were rinsed in water, optically observed, and the corrosion products identified by XRD as explained earlier.

Conflict of Interest

The authors declare no conflict of interest.

Data Availability Statement

Research data are not shared.

[1] R. O. Hussein, X. Nie, D. O. Northwood, *Materials* **2013**, *38*, 55.
[2] A. L. Yerokhin, L. O. Snizhko, N. L. Gurevina, A. Leyland, A. Pilkington, A. Matthews, *J. Phys. D: Appl. Phys.* **2003**, *36*, 2110.
[3] L. O. Snizhko, A. L. Yerokhin, A. Pilkington, N. L. Gurevina, D. O. Misnyankin, A. Leyland, A. Matthews, *Electrochim. Acta* **2004**, *49*, 2085.
[4] G. Sundararajan, L. R. Krishna, *Surf. Coat. Technol.* **2003**, *167*, 269.
[5] A. Ayday, M. Durman, *Phys. Pol. A* **2015**, *127*, 886.
[6] E. Matykina, R. Arrabal, P. Skeldon, G. E. Thompson, *Electrochim. Acta* **2009**, *54*, 6767.
[7] M. Montazeri, C. Dehghanian, M. Shokouhfar, A. Baradaran, *Appl. Surf. Sci.* **2011**, *257*, 7268.
[8] X. Liu, G. Li, Y. Xia, *Surf. Coat. Technol.* **2012**, *206*, 4462.
[9] M. Javidi, H. Fadaee, *Appl. Surf. Sci.* **2013**, *286*, 212.
[10] R. O. Hussein, X. Nie, D. O. Northwood, *Electrochim. Acta* **2013**, *112*, 111.
[11] R. Arrabal, E. Matykina, T. Hashimoto, P. Skeldon, G. E. Thompson, *Surf. Coat. Technol.* **2009**, *203*, 2207.
[12] N. Godja, N. Kiss, C. Löcker, A. Schindel, A. Gavrilovic, J. Wosik, R. Mann, J. Wendrinsky, A. Merstallinger, G. E. Nauer, *Tribol. Int.* **2010**, *43*, 1253.
[13] L. Famiyeh, X. Huang, *Mod. Concept Mater. Sci.* **2019**, *2*, 000526.
[14] E. Matykina, R. Arrabal, A. Mohamed, P. Skeldon, G. E. Thompson, *Corros. Sci.* **2009**, *51*, 2897–2905.
[15] V. Dehnavi, D. W. Shoesmith, B. L. Luan, M. Yari, X. Y. Liu, S. Rohani, *Mater. Chem. Phys.* **2015**, *161*, 49–58.
[16] R. O. Hussein, D. O. Northwood, *Production of Anti-Corrosion Coatings on Light Alloys (Al, Mg, Ti) by Plasma-Electrolytic Oxidation (Peo)*, IntechOpen, London, UK **2014**, pp. 202–238.
[17] X. Nie, E. I. Meletis, J. C. Jiang, A. Leyland, A. L. Yerokhin, A. Matthews, *Surf. Coat. Technol.* **2002**, *149*, 245.
[18] L. K. Mirelman, J. A. Curran, T. W. Clyne, *Surf. Coat. Technol.* **2012**, *207*, 66.
[19] S. Stojadinovic, N. Radic, R. Vasilic, M. Petkovic, P. Stefanov, Lj. Zekovic, B. Grbic, *Appl. Catal., B* **2012**, *126*, 334.
[20] A. Fujishima, X. Zhang, D. A. Tryk, *Surf. Sci. Rep.* **2008**, *63*, 515.
[21] N. Tadić, S. Stojadinović, N. Radić, B. Grbić, R. Vasilić, *Surf. Coat. Technol.* **2016**, *305*, 192.
[22] S. Franz, D. Perego, O. Marchese, A. Lucotti, M. Bestetti, *Appl. Surf. Sci.*, **2016**, *385*, 498.
[23] X. Nie, A. Leyland, A. Matthews, *Surf. Coat. Technol.* **2000**, *125*. 407.
[24] A. L. Yerokhin, X. Nie, A. Leyland, A. Matthews, *Surf. Coat. Technol.* **2000**, *130*, 195.
[25] D. Dzhurinskiy, Y. Gaob, W.-K. Yeung, E. Strumban, V. Leshchinsk, P.-J. Chua, A. Matthews, A. Yerokhin, R. Gr. Maev, *Surf. Coat. Technol.* **2015**, *269*, 258–265.
[26] A. L. Yerokhin, A. A. Voevodin, V. V. Lyubimov, J. Zabinski, M. Donley, *Surf. Coat. Technol.* **1998**, *110*, 140.
[27] A. Bahramian, K. Raeissi, A. Hakimizad, *Appl. Surf. Sci.* **2015**, *351*, 13.
[28] L. Liu, H. Zhao, J. M. Andino, Y. Li, *ACS Catal.* **2012**, *2*, 1817.
[29] X. Lu, M. Mohedano, C. Blawert, E. Matykina, R. Arrabal, K. U. Kainer, M. L. Zheludkevich, *Surf. Coat. Technol.* **2016**, *307*, 1165.
[30] V. Dehnavi, *PhD Thesis*, The University of Western Ontario, **2014**.
[31] X. D. Chen, Q. Z. Cai, L. S. Yin, *Adv. Mater. Res.* **2013**, *550–553*, 1969.
[32] X. Wang, X. Wu, R. Wang, Z. Qui, *Int. J. Electrochem. Sci.* **2013**, *8*, 4986.
[33] M. Mohedano, X. Lu, E. Matykina, C. Blawert, R. Arrabal, M. L. Zheludkevich, *Surf. Sci. Electrochem.* **2018**, 423.
[34] S. Ignjatović, C. Blawert, M. Serdechnova, S. Karpushenkov, M. Damjanović, P. Karlova, D. C. F. Wieland, M. Starykevich, S. Stojanović, L.j. Damjanović-Vasilić, M. L. Zheludkevich, *Appl. Surf. Sci.* **2021**, *544*, 148875.
[35] M. Treviño, N. F. Garza-Montes-de-Oca, A. Pérez, M. A. L. Hernández-Rodríguez, A. Juárez, R. Colás, *Surf. Coat. Technol.* **2012**, *206*, 2213.
[36] Y. Rodriguez-Jaimes, D. I. Naranjo, S. Blanco, S. J. García-Vergara, *J. Phys.: Conf. Ser.* **2017**, *935*, 012031.
[37] L. Rama Krishna, K. R. C. Somaraju, G. Sundararajan, *Surf. Coat. Technol.* **2003**, *163–164*, 484.
[38] C. Krywka, H. Neubauer, M. Priebe, T. Salditt, J. Keckes, A. Buffet, S. V. Roth, R. Doehrmann, M. Mueller, *J. Appl. Cryst.* **2012**, *45*, 85.
[39] RUFF sample data, integrated database of Raman spectra, X-ray diffraction and chemistry data for minerals, https://rruff.info/Rutile/R060745 (accessed: August 2020).
[40] RUFF sample data, integrated database of Raman spectra, X-ray diffraction and chemistry data for minerals, https://rruff.info/Anatase/R060277 (accessed: August 2020).